Copper/Nickel-Decorated Olive Pit Biochar: One Pot Solid State Synthesis for Environmental Remediation

Ahmed M Khalil, Laurent Michely, Rémy Pires, Stéphane Bastide, Khouloud Jlassi, Souad Ammar, Mohamed Jaziri, Mohamed M Chehimi

applied sciences

MDPI

Type of the Paper (Article.)

Copper/nickel-decorated olive pit biochar: One pot solid state synthesis for environmental remediation

Ahmed M. Khalil[1,2*], Laurent Michely[2], Rémy Pires[2], Stéphane Bastide[2*], Khouloud Jlassi[3], Souad Ammar[4], Mohamed Jaziri[5], Mohamed M. Chehimi[2,4,1]

[1] Photochemistry Department, National Research Centre, Dokki, 12622 Giza, Egypt
[2] Université Paris Est, CNRS, ICMPE (UMR 7182), 94320 Thiais, France
[3] Center for Advanced Materials, Qatar University, P.O. Box 2713, Doha, Qatar
[4] Université de Paris, CNRS, ITODYS (UMR 7086), 75013 Paris, France
[5] Laboratoire Electrochimie Et Environnement, Ecole Nationale d'Ingénieurs de Sfax, Université de Sfax, 3038 Sfax, Tunisia

Featured Application: Valorization of agrowaste biochar into catalytic material for environmental remediation potential application..

Abstract: Developing micro- and nanomaterials for environmental pollution remediation is hot topic presently. Among the plethora of strategies, designing supported nanocatalysts for the degradation of pollutants witnessed constant renewal. In this context, we are addressing one of the UN Sustainable Development Goals by valorizing agrowaste as a source of biochar which serves as support for bimetallic nanocatalysts. Herein, Olive pit powder particles were impregnated with copper and nickel nitrates and pyrolyzed at 400 °C. The resulting material consists of bimetallic CuNi-decorated biochar. CuNi nanocatalysts were found to be as small as 10 nm and very well dispersed over biochar with zero valent copper and nickel and formation of copper-nickel solid solutions. The biochar@CuNi exhibited typical soft ferromagnet hysteresis loops with zero remanence and zero coercivity. The biochar@CuNi was found to be efficient catalyst of the reduction of methyl orange (MO) dye, taken as model pollutant. To sum up, the one pot method devised in this work provided unique CuNi-decorated biochar and opens new horizons for the emerging topic of biochar-supported nanocatalysts.

Keywords: Agrowaste valorization; Olive pit; Biochar; CuNi bimetallic nanocatalyst; Methyl orange; Clean water and sanitation.

1. Introduction

Recently, the materials science community witnessed sky rocketing number of research papers on biochar. Search on Web of Science with keyword "biochar" returned the following results: 2 papers in 2001, 221 in 2011, 1413 in 2016, 4333 in 2020 and 3238 in 2021‡ which means that

‡ Last accessed 12 August 2021.

over 5000 papers should be published on the topic, by the end of 2021. This testifies for the vitality of this branch of materials sciences.

The rationale for the rush in research on biochar lies in the availability of biomass worldwide in different forms such as agrowastes, *i.e.* peels [1], leaves [2], palm fronds [3] and seeds [4]. The production of biochar depends on various parameters, the initial composition of the biomass [5] and the pyrolysis parameters [6]. Biochar production falls within the energy sector as it yields bio-oil and biogas on top of the biochar itself. Biochar is employed in agriculture for soil remediation and as adsorbent in environmental applications, *e.g.* removal of organic and inorganic pollutants. In the domain of materials science, biochar was found to be a unique source for making graphene [7] but raised much hope if valorized as support of nanocatalysts [8]. In the latter case, biochar is usually produced then post-treated for the immobilization of metal ions followed by in situ reduction therefore leading to immobilized nanocatalysts [9]. For other purposes, metal ions are loaded on the biochar (or other carbon allotrope) and calcined to provide immobilized metal oxide nanocatalysts [10].

In order to reduce the steps to biochar-immobilized nanocatalysts, we reasoned that the initial biomass could be loaded with metal ions and the modified biomass powder could be pyrolyzed in view of obtaining, in one step, nanocatalysts-coated biochar. This approach is attractive and has been seldom reported; it concerned the design of rice husk biochar-immobilized copper metallic nanocatalysts for the catalytic cracking of biomass primary tar [11]. As alternative methods, hydrothermal carbonization permitted to prepare hydrochar-immobilized copper nanoparticles in single step but this required long process time and additional $NaBH_4$ to reduce the metal ions [12]. Carbothermal production is another process which is mostly employed for recycling used batteries [13], though recently it has also been extended for designing carbon-loaded catalyst [14]. Olive stones are also widely valorized agrowastes, *e.g.* as biofillers for polymer composites [15, 16]. In 2017, some of us employed olive stone powders as biosourced cellulosic support of silver and gold nanoparticles and the final olive pit-supported nanocatalysts served for the degradation of para-nitrophenol [17]. Herein, we take advantage of this widely available agrowaste from Tunisia (a country in the top five producers of olive oil by volume [18]) to make nanocatalyst-decorated biochar. Instead of the noble metals silver and gold, we rather targeted copper-nickel bimetallic nanocatalysts. These supported bimetallic nanoparticles served as electrocatalysts for the reduction of nitrates in wastewater [19] and as heterogeneous catalysts for the reduction of dyes [20].

Herein, we bridge the gap between the use of olive pit powder particles as support of noble nanocatalyst and the unique, single step making of biochar-immobilized low-cost bimetallic copper-nickel nanocatalyst. The final copper/nickel-decorated olive pit biochar hybrid was characterized in terms of morphology, elemental and chemical composition, crystalline structure, thermal stability and response to magnetic field. It was then tested as potential heterogeneous catalyst of the discoloration of Methyl Orange aqueous solution. As it stands, this work fulfils three requirements: *(i)* valorization of agrowaste as biochar, *(ii)* biochar-supported nanocatalysts for dye degradation application, and *(iii)* tackling one of the United Nations' Sustainable Development Goals pertaining to environmental remediation and production of clean water.

2. Materials and Methods

2.1. Materials

Olive pit solid waste is an industrial by-product of olive oil extraction process from Tunisia. The remaining olive oil was further treated with hexane and the remaining solid olive waste dried to evaporate water. The resulting residue was cryo-ground to fine particles (in the 60–400 μm range) [15]. The OPs employed in this work contain fat and wax: 10; pectine: 6.6; lignin: 16; hemicellulose: 43; ash: 2; and cellulose: 22.4 wt.% as determined by French Standard method NFT12-011 (equivalent to ISO 638). $Cu(NO_3)_2,3H_2O$ and $Ni(NO_3)_2,6H_2O$ were purchased from Aldrich and used as received.

2.2. Preparation of metallic nanoparticle-coated biochar

Weighed olive pit particles were added to metallic salt solutions under stirring. The mixtures were stirred at RT for 30 minutes and then poured over a glass lens and left to dry overnight. Due to the very hydrophobic nature of olive pit particles [17], the metal salt solutions were prepared using ethanol as solvent.

The olive pit and metal ion salt mixtures were weighed again, and when steady state mass was noticed, subjected to pyrolysis in tube furnace (Thermolyne, model 21100) under nitrogen/hydrogen mixture (95/5 %). Table 1 reports the experimental conditions.

Table 1. Biochar loads and weights with copper and nickel: from the olive pit (OP) to the CuNi-decorated biochar, including pyrolysis conditions.

Materials	OP mass (g)	$Cu(NO_3)_2.3H_2O$ mass (g) / mmol	$Ni(NO_3)_2.6H_2O$ mass (g) / mmol	Solvent (ml)	Pyrolyzed OP + metal ion mixture (g)	Biochar mass (g) and yield (%)	Expected, final metal/biochar ratio (mmole/g)
Pyrolysis conditions: 30 °C/min ; T_{max}: 400 °C; Dwell time : 15 min.							
B	-	-	-	-	0.515	0.136 (26.4 %)	0
B@CuNi	3.670	0.843 / 3.489	1.007 / 3.463	Ethanol, 10	0.775	0.169 (21.9 %)	5.521 mmol/g
B@Cu	3.674	0.849 / 3.514	-	Ethanol, 10	1.192	0.372 (31.2 %)	2.489 mmol/g
B@Ni	3.67	-	1.012 / 3.480	Ethanol, 10	1.288	0.367 (28.5 %)	2.608 mmol/g

Materials characterization

SEM images and EDX spectra were acquired using a Zeiss Merlin Field Emission Scanning Electron Microscope operating at 5 kV (Oberkochen, Germany) coupled with a SDD X-Max from Oxford Instruments. In order to avoid static charge on surface, all samples were coated with a 3,0 nm thin layer of palladium using a Cressington 208HR sputter-coater coupled with a Cressington MTM-20 thickness controller.

TGA measurements were performed with a Setaram apparatus (Setsys Evolution model). The ramp was from RT to 800 °C at 10 °C/min heat rate.

The XRD pattern of all the prepared samples were recorded using a X'Pert-Pro Panalytical diffractometer equipped with a Cobalt X-ray source (λ = 1.7889 Å) and operating in the reflexion Bragg-Brentano geometry.

Magnetic measurements were conducted at room temperature on a Vibrating Sample Magnetometer (VSM) from QUANTUM DESIGN.

Biochar sample was characterized using Horiba HR 800 apparatus fitted with a He–Ne laser beam the wavelength of which was set at 514 nm.

Catalysis assays

Catalytic reduction of methyl orange was conducted in the following conditions. In a 1 cm length quartz cuvette, 4 ml of 20 ppm Methyl Orange solution was incubated with 1 mg B@CuNi. The mixture was sonicated in water bath for 2 min then 30 mg $NaBH_4$ were added to proceed with catalysed discoloration reaction. UV-vis spectra were recorded using Varian Cary 50 Bio apparatus.

3. Results

3.1. General strategy of the work

Several methods of making biochar from various sources have recently been summarized [6].The route for biochar is depicted in Figure 1a (upper panel): olive pit powder is the source of biomass, pyrolysis is the type of treatment and biochar stands for the main product. Slow and mild pyrolysis conditions were adopted: 30 °C/min heating under nitrogen/H_2 (5%) atmosphere with a dwell time of 15 min at 400 °C prior to cooling at RT. 400 °C ensures a maximal biochar yield whilst H_2 was employed in order to ensure metal ion reduction to metallic state. Figure 1, lower panel, displays the digital photographs of olive pit powder (Figure 1b), the same powder impregnated with copper and nickel nitrates mixture (Figure 1c), olive pit biochar (Figure 1d) and biochar-supported CuNi nanoparticles (Figure 1e).

It is interesting to note that due to nickel, the copper-nickel alloy-decorated biochar (B@CuNi) is magnetic and could be attracted by a magnet (Figure 1f, and Video S1, also available at https://vimeo.com/563456328).

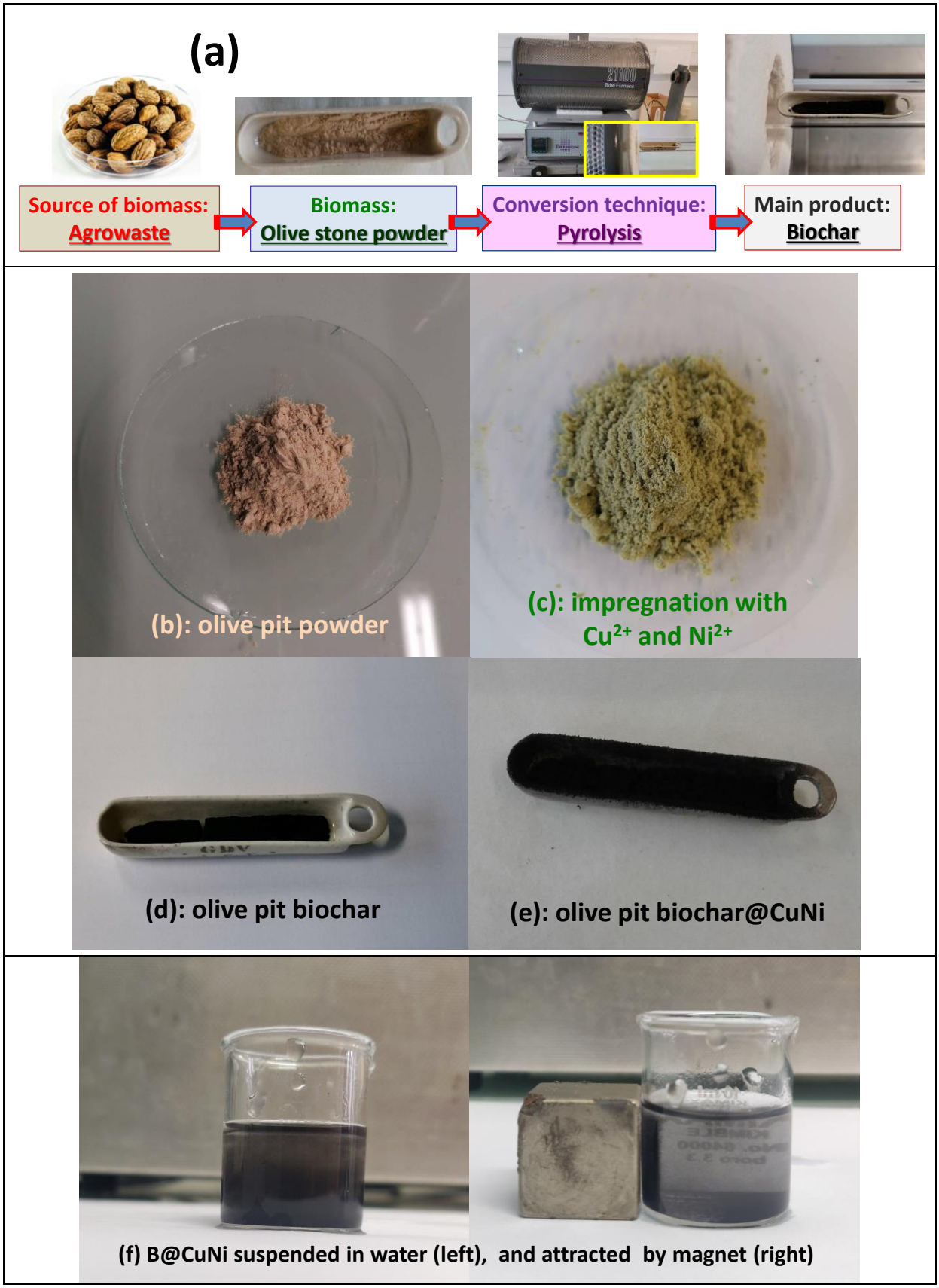

Figure 1. (a) Upper panel showing route for making biochar from olive pit biochar. Middle panel shows digital photographs of (b) olive pit powder, (c) olive pit powder after impregnation of copper and nickel nitrates, (d) the olive pit biochar, and (e)

CuNi-decorated biochar obtained by direct pyrolysis of powder shown in (c). Lower panel: (f) digital pictures showing suspension of B@CuNi before (left) and after attraction by a magnet (right).

3.2. Surface morphology and elemental analysis

Figure 2 displays SEM images of pristine and decorated biochar samples. Figure 2a depicts the surface morphology of CuNi-decorated biochar. It shows a porously extending surface area for the nanocatalyst-decorated biochar. CuNi nanoparticles spread along the top of the carbonaceous sample. Upon magnifying the SEM image to provide more comprehensive information, a clearer distribution for the metallic nanoparticles can be observed as shown in Figure 2b. It is advantageous to notice CuNi nanoparticles covering the inner surface of the pores of biochar in the form of light spots onto the inner denser surface; as surrounded by a circle and ellipse in Figure 2b. CuNi nanoparticles appear as distinct spheres avoiding any aggregates that may arise in such cases as illustrated in the inset of Figure 2c. They provide spherical, undeformed structure for the provided nanoparticles. Upon comparing B@CuNi surface to that of the pristine biochar, less number of pores can be visualized on the surface as displayed in Figure 2d. These pores manifest evidently at higher magnification as illustrated in Figure 2e in a smaller proportion when compared to the CuNi-biochar sample. The inset in Figure 2f is mentioned here as a reference sample in the absence of CuNi supporting catalyst. The bare biochar micrograph denotes a plain surface without much informative morphology and its porous structure cannot be recognized easily.

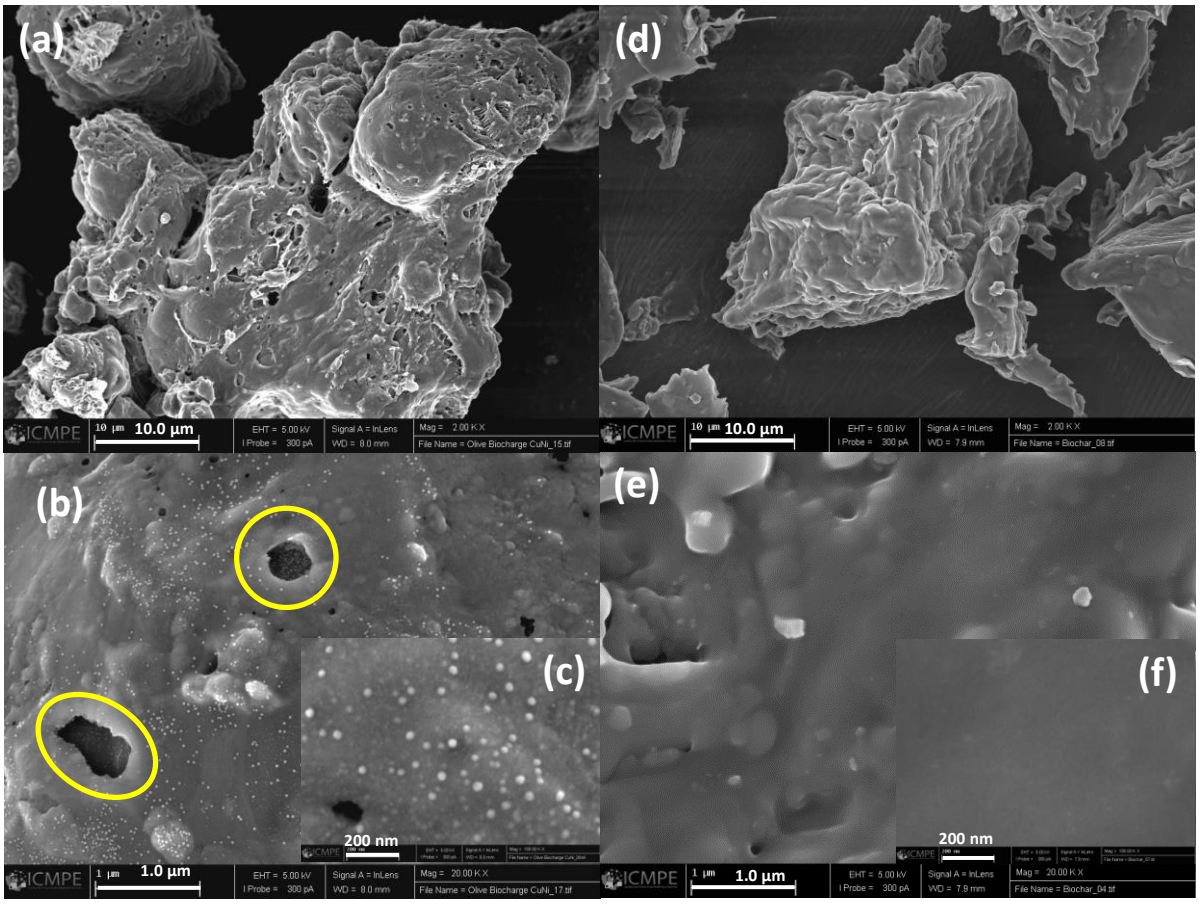

Figure 2. SEM images of biochar/CuNi hybrid (a-c) and the reference pristine biochar (d-f) without any supported nanocatalysts, at indicated magnifications. Some pores (in b) enriched with CuNi nanoparticles are surrounded by a circle and an ellipse.

EDX was used to determine the surface composition of B@CuNi over several spots. For comparison, we have also recorded EDX spectra for OP impregnated with metal salts, and the bare OPs. Figure 3a-c display EDX spectra of Ops, OP@metal salts and B@CuNi. Elemental composition for B@CuNi is displayed in Figure 3d, whereas (Cu+Ni)/(C+O) and Cu/Ni atomic ratios are compared in Figure 3e for and OP@metal salts and B@CuNi. Figures 3a-c conclusively show the absence of any copper and nickel ions from the surface of Ops, whereas the characteristic Cu and Ni peaks are noted on the impregnated OP particles with peak intensity increasing in the order Cu~Ni < O < C. Increase in the O/C peak intensity ratio is due to the hydrated metal nitrates. Upon pyrolysis, the metal nitrate-impregnated OPs are transformed into metallic alloy-decorated biochar B@CuNi with relative peak intensity increasing in the order O < Cu~Ni < C. Quantitatively, Figure 3d displays C, O, Cu and Ni atomic % at 15 spots from B@CuNi powder sample; composition is fairly the same from one spot to another which indicates even decoration of the biochar with metallic nanoparticles. This is due to homogenous impregnation of the OPs with metal nitrates. (Cu+Ni)/(C+O) atomic ratio (Figure 3d) increases on going from OP@metal salts to B@CuNi due to the pyrolysis of the olive stones and subsequent release of water and nitrates. Figure 3e shows that Cu/Ni atomic ratio remains the same

within standard deviation for OP@metal salts (1.00±0.10) and B@CuNi (1.125±0.277). The Cu/Ni ratio obtained for B@CuNi accounts for the equimolar impregnation of olive pits by metal ions.

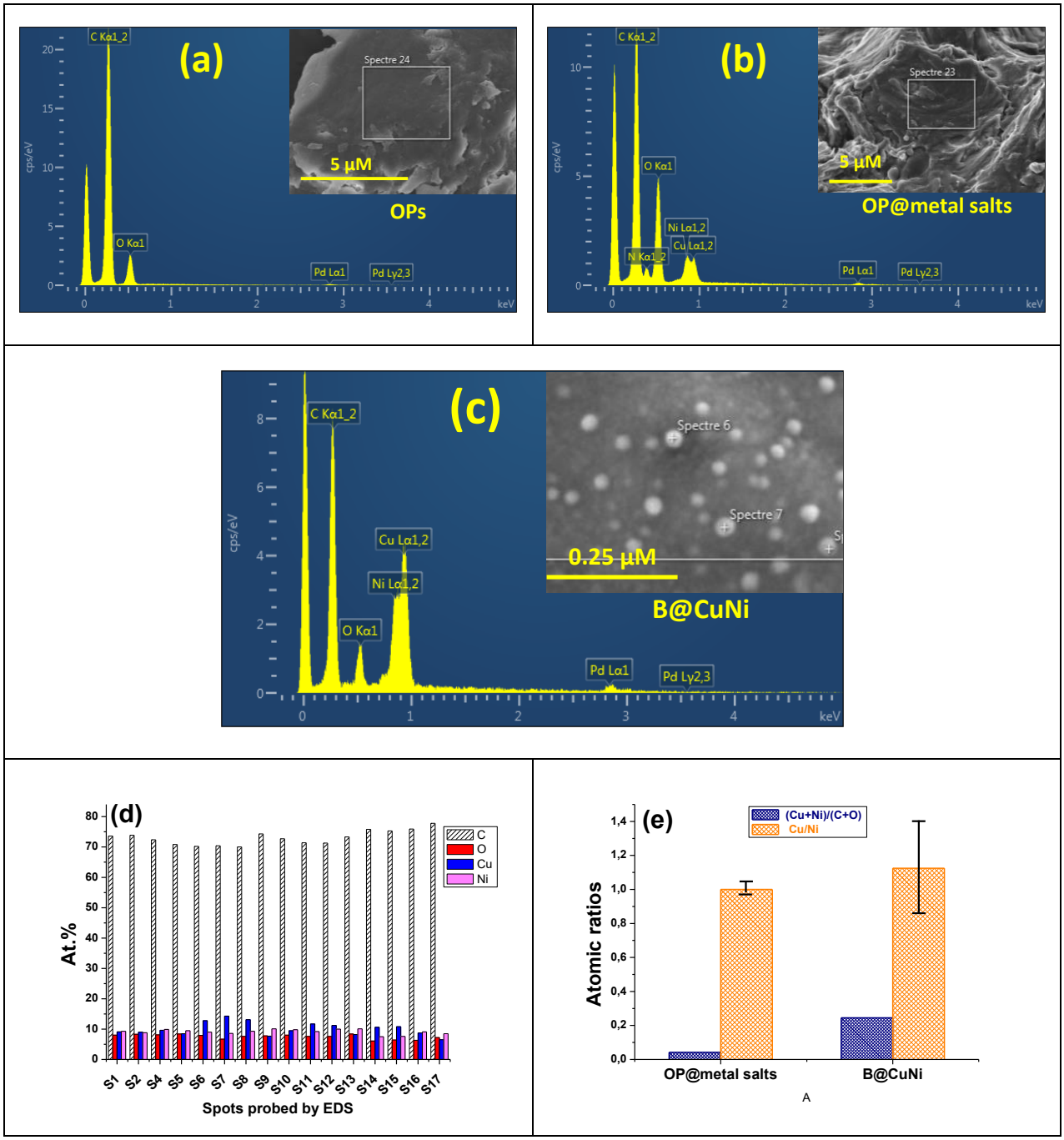

Figure 3. EDX spectra of (a) olive pit powder particles, OPs; (b) Ops impregnated with metal salts (copper and nickel nitrates), and (c) B@CuNi. SEM images show spots probed for the acquisition of EDX spectra. EDX quantification: (d) elemental analysis of C, O, Cu and Ni detected at 15 spots of B@CuNi surface; and (e) (Cu+Ni)/(C+O) and Cu/Ni atomic ratios averaged over 15 spots.

3.3. Phase analysis

The prepared catalysts were analysed using both XRD and Raman to identify the nature of the metal and carbon contents, respectively. Figure 4 displays XRD patterns of B@CuNi and of the reference materials Biochar and B@Ni. Those of B@Ni and B@Cu (not shown) correspond very well to the structures of nickel and copper face centered cubic metals (ICDD n°98-004-1508 and 98-005-2256), respectively. The XRD pattern of B@CuNi exhibits the same type of diffraction lines but at 2θ positions located between those of pure Cu an pure Ni phases, suggesting that the biochar serves as support of a $Ni_{1-x}Cu_x$ metallic solid solution. This is strong supporting evidence that copper and nickel were alloyed during the one-step pyrolysis process. Moreover, it is noteworthy that all peaks are broadened which is in line with the production of small crystals that were imaged by SEM (see Figure 2b,c). However, as the technique probes the bulk, no surface oxidation of the nanocatalysts was detected. This would best be done using the more specific technique X-ray photoelectron spectroscopy (XPS). Indeed, elsewhere, surface oxidation of nickel [21], copper [21, 22] and iron [14] loaded on biochar was detected; as well as partial oxidation of palladium nanoparticles loaded on organo-functionalized mesoporous silica [23].

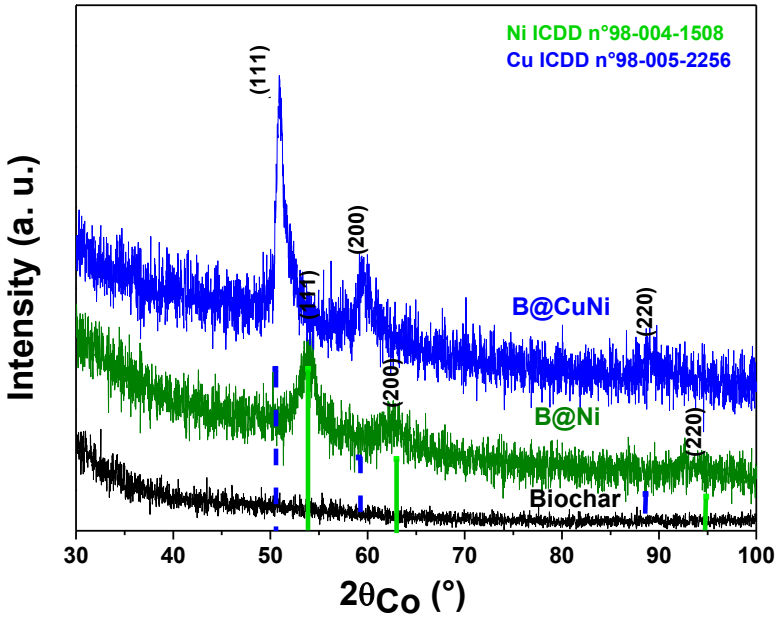

Figure 4. XRD-patterns of B@Ni and B@CuNi samples compared to that of free biochar. The tabulated peak positions of bulk Ni (ICDD n°98-004-1508) and Cu phases (98-005-2256) are given for information.

The formation of metallic Ni and CuNi particles was also confirmed by the measurement of the variation of the sample magnetization M as a function of the magnetic field H at room temperature. Indeed, by cycling the magnetic field H between -20.0 and +20.0 kOe, typical soft ferromagnet hysteresis loops with zero remanence and zero coercivity [24], were recorded on both B@CuNi and B@Ni samples (Figure 5). This feature must be underlined since it accounts for the capability of the designed catalysts to be reversibly

attracted by an external magnetic field making their recovering and reuse easy to achieve. Interestingly, as the copper alloyed nickel particles are usually less magnetic than the nickel pure one, one may notice on the recorded M(H) plots that the saturation magnetization of B@Ni is much more quickly reached than that of B@CuNi.

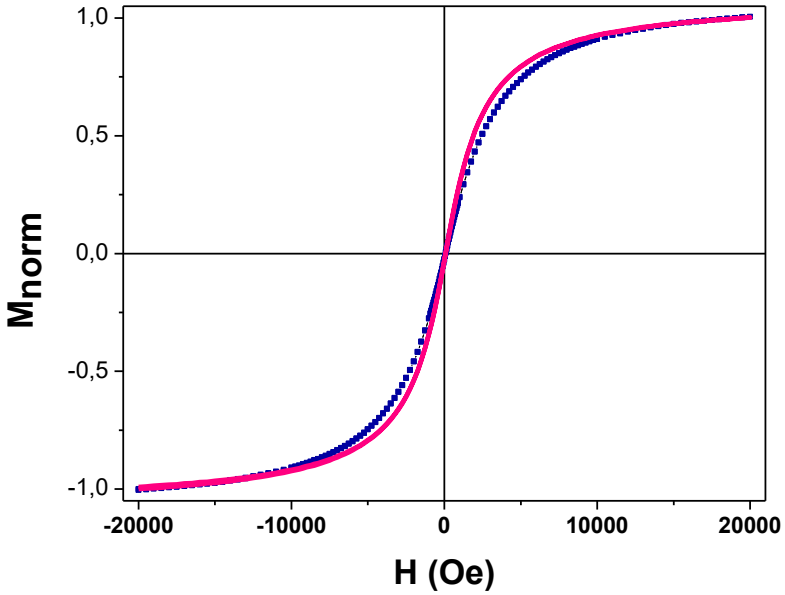

Figure 5. Variation of the normalized magnetization as a function of the magnetic field at room temperature on B@Ni (—) and B@CuNi (■).

To complete these structural characterizations, Raman spectroscopy was carried out on the prepared sample with a special emphasis on their carbon signature. The spectrum recorded in the 1000-2000 cm^{-1} energy region for the metal-free Biochar is shown in Figure 6 to illustrate this purpose. It is fitted with five components assigned to S (1262 cm^{-1}; sp^2-sp^3),
D (1380 cm^{-1}; sp^2, C-C between aromatic cycles and highly ordered carbon material),
V (1506 cm^{-1}; sp^2-sp^3, amorphous carbon structures), G (1596 cm^{-1}; graphite, sp^2) and
G_L (1696 cm^{-1}; sp^2, C=O) [25, 26]. Particularly, the D and G bands are assigned to disordered and ideal graphitic lattice, respectively. The D/G peak height and ratios area ratios equal 0.66 and 0.87, respectively. The spectrum indicates therefore the presence of C sp^2 atoms, but without any excess of amorphous sp^3 hydrocarbons. It is to note that the D/G ratio, referring to the degree of defects in the carbon material, is much lower than those reported for hydrothermally synthesized graphene quantum dots [27]. It is also lower than the values reported for pruning wastes of apple trees post-treated at 400 °C (D/G height ratio ~ 0.72) [28], ferrate-activated porous biochar prepared at 900 °C (D/G height ratio= 1.07) [29], and (D/G height ratio= 1.14) [30]. This is important when considering low pyrolysis temperature and high yield we have obtained, as well as relatively higher graphitization.

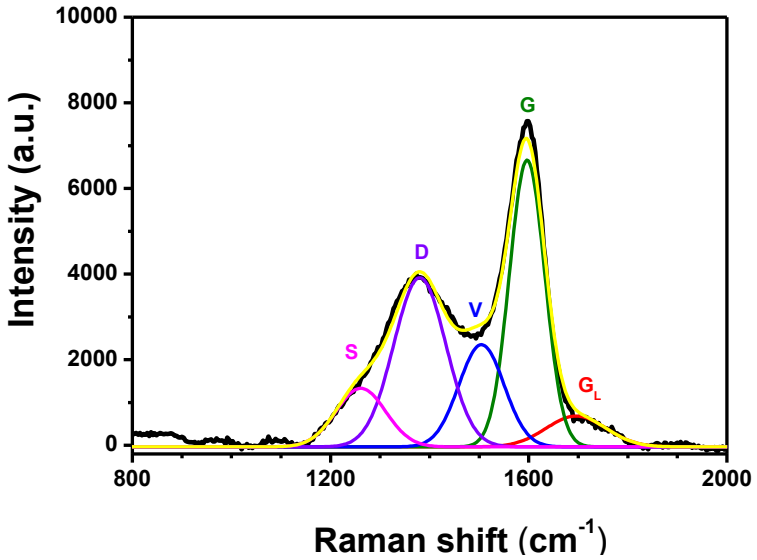

Figure 6. Peak-fitted Raman spectrum of olive pit biochar.

3.3. Thermal stability

Thermogravimetric analysis (TGA) was utilized as a substantial technique to monitor the thermal stability of biochar and match it with CuNi-decorated biochar. For comparison, we have also plotted the thermograms of B@Cu and B@Ni prepared with single metal ion nitrate. The sequence of residual weight % at high temperature is Biochar < B@Ni < B@Cu < B@CuNi. This is logical sequence as under air biochar is burnt out, whereas with nickel the final biochar is loaded with metallic nickel which converts to NiO. Copper converts to CuO and as both copper and nickel nitrates were impregnated at equal number of moles per gram of biomass, it is logical to obtain slightly higher weight % for B@Cu compared to B@Ni. With increased final number of moles per gram of biochar (see Table 1), biochar burns out but not CuNi alloy which converts to oxides, hence higher weight % for B@CuNi (lower weight loss). In the literature, carbon@Cu and carbon@Ni prepared by annealing of the corresponding metal organic frameworks showed only slight decrease in weight loss because TGA was conducted under inert atmosphere [20]. In contrast, biochar loaded with a copper complex catalyst exhibited substantial weight loss under air, with steady state reached around 500 °C and final 50% weight [31]. As far as nickel-biochar based magnetic catalyst is concerned, weight loss of 49.8 % was reported at 800 °C, presumably under air but this was not specified [32].

Returning to the main hybrid B@CuNi and reference material Biochar, both samples show a comparable behaviour of thermal stability till reaching 240 °C for steady samples withstanding temperature as shown in Figure 7. Thermogravimetric analysis was carried under air. A slight increase of the weight of the pristine biochar sample is observed at 280 °C; this is correlated to the oxidation of both biochar and the metal alloy. It might have influenced the biochar specimen and led to a slight increase in its weight%. At higher temperatures, biochar started to decompose at 330-340 °C till reaching 500 °C.

For B@CuNi, a plateau region was reached and corresponds to 42 % residual weight of the original sample. The sample retained its thermal stability up to 270-280 °C then a decomposition step occurred at elevated temperatures to reach steady state at 455 °C with a residual weight of 45% of the original weight, higher than that of biochar due to loaded metallic nanoparticles [20].

On a quantitative viewpoint, the thermograms were obtained under air which suggests formation of CuO and NiO and the weight % differences between pristine and decorated biochar should account for the oxides. B@Cu has a residual weight of 32.6% and that of biochar 12.5 %. The difference of 20.1 % accounts for CuO, that is 0.201 g CuO for 1g of hybrid biochar B@C which corresponds to 2.53 mmol Cu per gram of hybrid biochar. This is matching the value of 2.489 mmol/g reported in Table 1, corresponding to an error of 1.6%. With the same reasoning, and by subtracting residual mass of biochar to that of B@Ni, one obtains 2.45 mmol nickel per gram of hybrid biochar, that is 6% less than the value of 2.608 mmol nickel/g B@Ni. Finally, concerning B@CuNi and assuming initial exact number of moles of nickel and copper nitrates (they differ by only 1%, see Table 1), the weight % difference with biochar equals to 44.5-12.5=32 %, *i.e.* 0.32 g of NiO/CuO mixture (for Ñi/Cu equimolar ratio) per 1 g hybrid biochar. Assuming a hypothetical oxide $CuNiO_2$ (molar mass = 154.2 g), one would get 4.15 mmol of copper-nickel mixture, that is 25% less total number of moles compared to the expected value reported in Table 1 (5.521 mmol/g). This apparent discrepancy could be due to incomplete oxidation of larger nanoparticles and possible segregation of one of the metals to the surface of the alloy nanoparticles [33]. This hypothesis requires a full investigation which is beyond the scope of this paper.

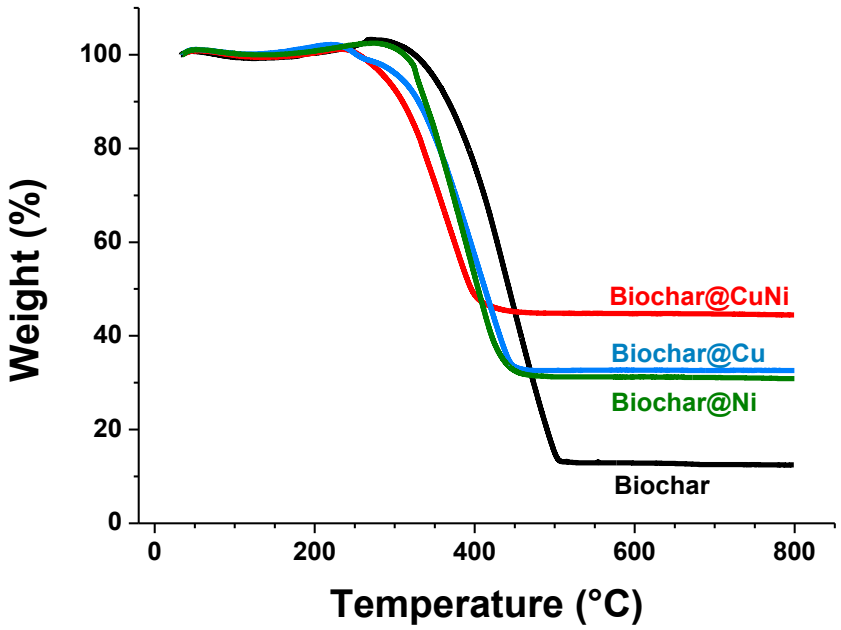

Figure 7. TGA plots recorded under air for biochar and B@CuNi.

3.4. Potential application: proof of concept of heterogeneous catalyzed degradation of methyl orange dye

Dye removal can be achieved through various routes comprising adsorption [34], filtration [35] or catalyzed degradation [36, 37]. Herein, we focus on the catalyzed degradation of MO in aqueous solution in order to assess the catalytic activity of the actual CuNi-decorated biochar. This process was carried out in the presence of $NaBH_4$ as reducing agent. Upon starting at time = 0 sec, the investigated samples did not show any significant changes in color of tested vials as illustrated in the upper row in Fig. 8a. After 30 min, the color of the solution loaded with decorated biochar turned to be colorless referring to decomposed MO (Fig. 8b). UV-vis spectra of MO with different reactants in the presence and absence of the decorated biochar are illustrated in Fig. 8c. Starting with the spectrum showing peaks with the highest intensity among the explored samples, MO displays a typical intense peak at 464 nm accompanied with a lower one at 270 nm. The first peak can be correlated to the conjugation of electron donor N=N bond. Meanwhile, the latter peak is featured to aromatic pi-pi* transition [38]. After diluting MO with deionized water, the same behaviour for absorbance bands arose, however with lower peak intensities. This may be referred to the dilution effect resulting from introducing water to the previously tested MO aqueous solution. The dilution step was implemented to confirm the presence of MO in the solution even at lower concentration with weaker absorption bands. Upon investigating the samples of MO with either CuNi-decorated biochar or $NaBH_4$ separately, the absorption peaks showed neither significant changes, nor shifts. Upon testing MO with B@CuNi and $NaBH_4$, the solution became transparent; this testifies for the degradation process of MO. The previously mentioned peaks vanished and new bands appeared at 245 and 248 nm. Accordingly, a cleavage of –N=N- bond took place to generate -NH_2 group. Hence, the newly formed species, namely sulfanilic acid and p-amino dimethylaniline, respectively [39, 40]. It is to note that no centrifugation was required to split the biochar and the supernatant; the latter was sedimented easily using a magnet, which facilitated sampling the supernatant for UV-vis analysis.

These preliminary results are encouraging as test dye aqueous solution containing ~0.24 µmol MO was discolored in less than 30 min using ~5.5 µmol of alloyed Cu and Ni metals, but the turnover number should be limited to the copper and nickel atoms present at the surface of the bimetallic nanoparticles thus resulting in higher TON value. The recovered B@CuNi hybrid catalyst permitted to catalyze the discoloration of a new, freshly prepared MO solution. This is due to the presence of NBH_4 which could reduce NiO and CuO if they are ever present at the surface of B@CuNi.

To finish, we are presently testing new processes for making biochar@CuNi that permit faster discoloration of MO solutions (within 1-10 min). The new studies need to be double checed and confirmed prior to future publication.

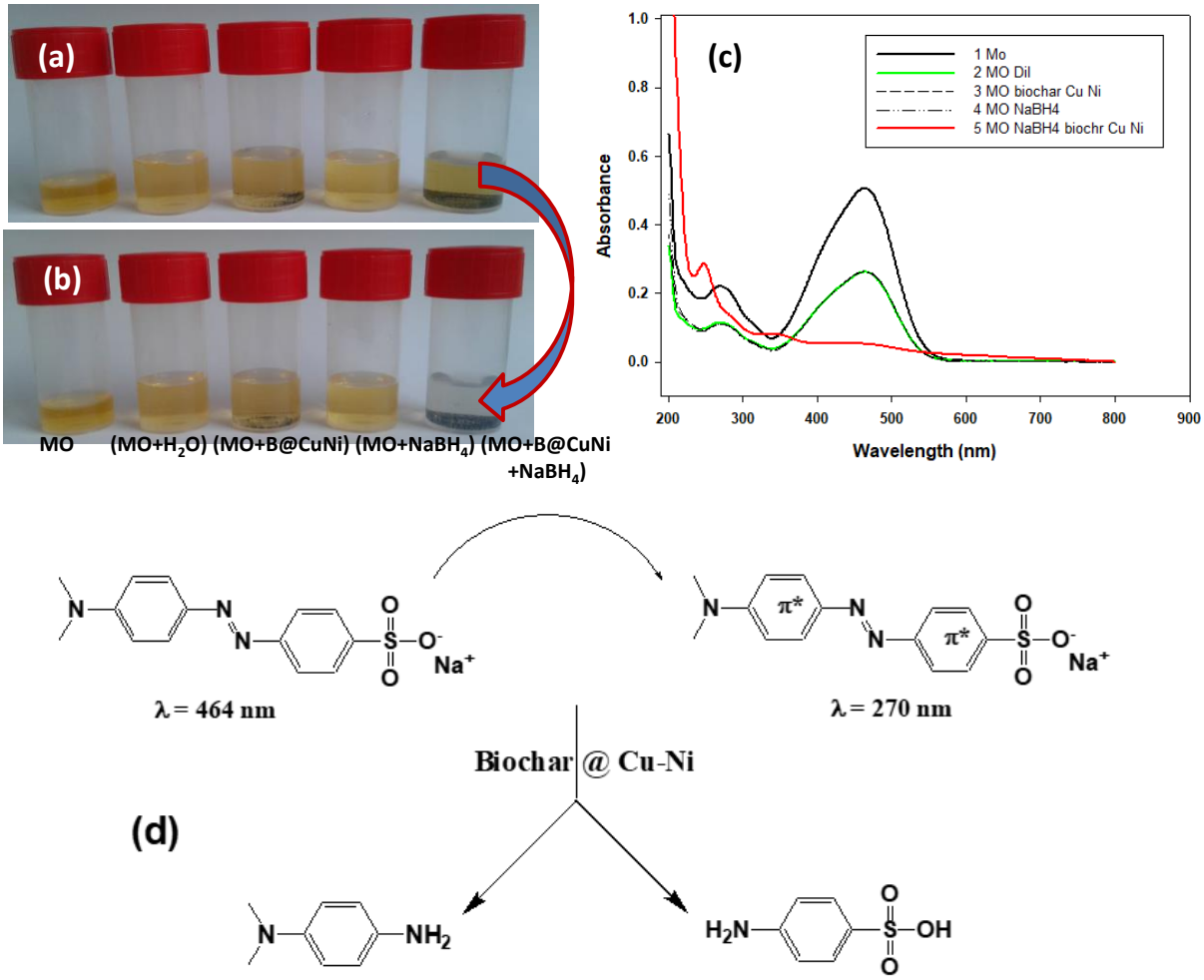

Figure 8. (a,b) Digital photographs and (b) UV-vis spectra for MO vials before and after catalytic reaction. (d) A proposed scheme for MO before and after the catalytic degradation with decorated CuNi-biochar.

Conclusion

We have composed a boosted biochar derived from an agrowaste; olive pit (OP) powder. Metallic salts of hydrated nickel and/or copper nitrate(s) as precursors were mixed with OP followed by pyrolysis, in one step at 400 °C to generate biochar@CuNi (B@CuNi). The resulting biochar was characterized by (SEM) to show a homogenous surface with well distributed CuNi nanoparticles onto the surface of the biochar. EDX and XRD asserted the formation of CuNi nanoparticles as metallic alloy decorating the biochar. Magnetization experiments accounted for the presence of nickel and demonstrated that nanocatalyst-decorated biochars behave as ferromagnets. B@CuNi showed a high catalytic performance in decomposing methyl orange (MO) dye.

The significance of this work lies in the valorization of agrowaste in general, and the production of an enhanced biochar decorated with bimetallic nanocatalyst (CuNi) in a facile process, in particular. This strategy of making nanocatlyst-doped biochar opens new avenues for water treatment and therefore, attempting to elegantly contribute in environmental remediation and thus to address UN Sustainable Development Goal 6 pertaining to clean water and sanitation.

Authors' contributions: Conceptualization (MMC and AMK); Methodology (MMC, AMK, SB); Validation (all authors); Formal Analysis and Investigation (all authors);
Writing-Original Draft (MMC and AMK); Writing - Review & Editing (all authors); Resources (MMC, LM, SB, RP, SA); Supervision (MMC); Funding acquisition (AMK, MMC).

Funding

AMK and MMC would like to thank both the French and Egyptian Governments for funding AMK's contribution through a fellowship granted by the French Embassy in Egypt (Institut Francais d'Egypte) and Science and Technology Developing Fund (STDF)-Egypt, Project number (42248).

Institutional Review Board Statement: Not applicable
Informed Consent Statement: Not applicable.
Data Availability Statement: Original data available on request. They are not archived in any repository.

Acknowledgements

Mrs Stépahnie Lau-Truong is acknowledged for Raman analysis.

Conflict of interest: the authors declare no conflict of interest

References

[1] A.G. Adeniyi, J.O. Ighalo, D.V. Onifade, Chemistry Africa 3 (2020) 439-448.

[2] M. Azeem, T.U. Hassan, M.I. Tahir, A. Ali, P.G.S.A. Jeyasundar, Q. Hussain, S. Bashir, S. Mehmood, Z. Zhang, Applied Soil Ecology 157 (2021) 103732.

[3] M. Zubair, N.D. Mu'azu, N. Jarrah, N.I. Blaisi, H.A. Aziz, M. A. Al-Harthi, Water, Air, & Soil Pollution 231 (2020) 1-19.

[4] A. Bagheri, E. Abu-Danso, J. Iqbal, A. Bhatnagar, Environmental Science and Pollution Research 27 (2020) 7318-7327.

[5] X. Sun, R. Shan, X. Li, J. Pan, X. Liu, R. Deng, J. Song, Gcb Bioenergy 9 (2017) 1423-1435.
[6] M. Tripathi, J.N. Sahu, P. Ganesan, Renewable and Sustainable Energy Reviews 55 (2016) 467-481.
[7] D.X. Luong, K.V. Bets, W.A. Algozeeb, M.G. Stanford, C. Kittrell, W. Chen, R.V. Salvatierra, M. Ren, E.A. McHugh, P.A. Advincula, Nature 577 (2020) 647-651.
[8] R.P. Lopes, D. Astruc, Coordination Chemistry Reviews 426 (2021) 213585.
[9] Y. Shen, P. Zhao, Q. Shao, F. Takahashi, K. Yoshikawa, Applied Energy 160 (2015) 808-819.
[10] G. Tan, Y. Wu, Y. Liu, D. Xiao, Journal of the Taiwan Institute of Chemical Engineers 84 (2018) 85-92.
[11] F. Guo, K. Peng, S. Liang, X. Jia, X. Jiang, L. Qian, Energy 180 (2019) 584-593.
[12] X. Ge, M. Ge, X. Chen, C. Qian, X. Liu, S. Zhou, Molecular Catalysis 484 (2020) 110726.
[13] S. Yeşiltepe, M. Buğdaycı, O. Yücel, M.K. Şeşen, Batteries 5 (2019) 35.
[14] V. Tamborrino, G. Costamagna, M. Bartoli, M. Rovere, P. Jagdale, L. Lavagna, M. Ginepro, A. Tagliaferro, Fuel 296 (2021) 120693.
[15] M. Khemakhem, M. Jaziri, Polymer Engineering & Science 56 (2016) 27-35.
[16] A.M. Khalil, K.F. El-Nemr, M.L. Hassan, Journal of Polymer Research 26 (2019) 1-11.
[17] S. Belbekhouche, S.I. Kebe, S. Mahouche-Chergui, M. Guerrouache, B. Carbonnier, M. Jaziri, M.M. Chehimi, Colloids and Surfaces A: Physicochemical and Engineering Aspects 529 (2017) 541-549.
[18] D. Fernández-Uclés, S. Elfkih, A. Mozas-Moral, E. Bernal-Jurado, M.J. Medina-Viruel, S. Ben Abdallah, Agriculture 10 (2020) 391.
[19] P. Mirzaei, Préparation de matériaux d'électrode pour l'élimination et la valorisation de polluants azotés, Paris Est, 2018.
[20] M.A. Ahsan, V. Jabbari, A.A. El-Gendy, M.L. Curry, J.C. Noveron, Applied Surface Science 497 (2019) 143608.
[21] C. Zhu, H. Wang, H. Li, B. Cai, W. Lv, C. Cai, C. Wang, L. Yan, Q. Liu, L. Ma, ACS Sustainable Chemistry & Engineering 7 (2019) 19556-19569.
[22] W.-J. Liu, K. Tian, H. Jiang, H.-Q. Yu, Green Chemistry 16 (2014) 4198-4205.
[23] A. Saad, C. Vard, M. Abderrabba, M.M. Chehimi, Langmuir 33 (2017) 7137-7146.
[24] M. Luo, C. Huang, F. Chen, C. Chen, H. Li, Journal of Dispersion Science and Technology (2020) 1-13.
[25] Y. Shao, C. Guizani, P. Grosseau, D. Chaussy, D. Beneventi, Carbon 129 (2018) 357-366.
[26] X. Li, J.-i. Hayashi, C.-Z. Li, Fuel 85 (2006) 1509-1517.
[27] X. Xiao, B. Chen, Environmental science & technology 51 (2017) 5473-5482.
[28] D.-G. Kim, S.-O. Ko, Chemical Engineering Journal 399 (2020) 125377.
[29] N. Thi Minh Tam, Y. Liu, H. Bashir, Z. Yin, Y. He, X. Zhou, International journal of environmental research and public health 17 (2020) 291.
[30] L.W. Endler, F. Wolfart, A.S. Mangrich, M. Vidotti, L.F. Marchesi, Chemical Papers 74 (2020) 1471-1476.
[31] P. Moradi, M. Hajjami, B. Tahmasbi, Polyhedron 175 (2020) 114169.
[32] P. Moradi, M. Hajjami, New Journal of Chemistry 45 (2021) 2981-2994.
[33] P.H.K. Charan, G.R. Rao, Microporous and mesoporous materials 200 (2014) 101-109.
[34] A.M. Khalil, S.H. Kenawy, Acta Chimica Slovenica 67 (2020) 96-104.
[35] A.E. Abdelhamid, A.A. El-Sayed, A.M. Khalil, Journal of Polymer Engineering 40 (2020) 833-841.
[36] Z. Ait-Touchente, A.M. Khalil, S. Simsek, S. Boufi, L.F.V. Ferreira, M.R. Vilar, R. Touzani, M.M. Chehimi, Cellulose 27 (2020) 1085-1097.
[37] F. Mousli, A.M. Khalil, F. Maurel, A. Kadri, M.M. Chehimi, Cellulose 27 (2020) 7823-7846.

340 [38] L. Yang, Q. Wang, J.R. Rangel-Mendez, F. Jia, S. Song, B. Yang, Materials Chemistry and Physics 246 (2020)
341 122829.
342 [39] E.M. Bakhsh, S.A. Khan, H.M. Marwani, E.Y. Danish, A.M. Asiri, S.B. Khan, International journal of biological
343 macromolecules 107 (2018) 668-677.
344 [40] Y. Sha, I. Mathew, Q. Cui, M. Clay, F. Gao, X.J. Zhang, Z. Gu, Chemosphere 144 (2016) 1530-1535.

345

346